

Article

Effects of Ti/N Ratio on Coarse-Grain Heat-Affected Zone Microstructure Evolution and Low-Temperature Impact Toughness of High Heat Input Welding Steel

Jin Liu ^{1,2,*}, Jiaji Wang ^{1,2}, Fengya Hu ^{1,2}, Kuijun Fu ^{1,2}, Zhiqiang Zhang ^{1,2} and Yumin Wu ^{1,2}

¹ State Key Laboratory of Metal Material for Marine Equipment and Application, Anshan 114021, China; agwj2013@163.com (J.W.); hfy312@126.com (F.H.); agfkj63@163.com (K.F.); lnkdzzq@126.com (Z.Z.)

² Research Institute of Ansteel Group, Anshan 114021, China

* Correspondence: liujin_ansteel@163.com; Tel.: +86-156-4121-4789

Abstract: Coarse-grain heat-affected zone (CGHAZ) properties of steel deteriorate when it is welded using high heat input, which always restricts the promotion and use of high heat input welding steel. TiN particles significantly inhibit the growth of austenite and improve the microstructure and properties of high heat input welding steel. Effects of different Ti/N ratios on the CGHAZ microstructure and properties of high heat input welding steel were studied using welding thermal simulations and in situ observations. Results showed that a higher Ti/N ratio led to the abnormal growth of austenite grains and promoted the nucleation and growth of lath ferrite, which made the microstructure of the CGHAZ heterogeneous. In contrast, austenite grains were more uniform at a lower Ti/N ratio. Thus, the microstructure was refined, the brittle structure was reduced, and the properties of the CGHAZ were improved. In addition, when Ti/N = 5.85, the impact absorption energy of the CGHAZ obviously fluctuated. However, when Ti/N = 2.82, the impact absorption energy of the CGHAZ was higher and more stable. These results provided a new idea for the development of high heat input welding steel based on TiN theory.

Keywords: Ti/N ratio; CGHAZ; welding thermal simulation; in situ observation



Citation: Liu, J.; Wang, J.; Hu, F.; Fu, K.; Zhang, Z.; Wu, Y. Effects of Ti/N Ratio on Coarse-Grain Heat-Affected Zone Microstructure Evolution and Low-Temperature Impact Toughness of High Heat Input Welding Steel. *Coatings* **2023**, *13*, 1347. <https://doi.org/10.3390/coatings13081347>

Academic Editor: Ramachandran Chidambaram Seshadri

Received: 26 June 2023

Revised: 26 July 2023

Accepted: 27 July 2023

Published: 31 July 2023



Copyright: © 2023 by the authors. Licensee MDPI, Basel, Switzerland. This article is an open access article distributed under the terms and conditions of the Creative Commons Attribution (CC BY) license (<https://creativecommons.org/licenses/by/4.0/>).

1. Introduction

Steel is the most important structural material, and is widely used in the fields of national energy development, infrastructure construction and machinery manufacturing [1,2]. With the increase in steel thickness, the industry is more inclined to adopt high heat input welding technology in order to improve production efficiency. For steel with significant thickness, such as ship plate steel, bridge steel and tank steel, multi-layer and multi-pass welding is required if a small heat input, such as manual welding, argon arc welding or gas-shielded welding, is used for welding. This consumes significant manpower and material resources. If high heat input welding technology is adopted, thick steel can be welded in one pass to greatly improve welding efficiency. Therefore, it has gradually become a trend to develop steel suitable for high heat input welding technology to replace traditional steel [3,4].

Although high heat input welding can improve production efficiency and reduce cost, it has many problems. With the increase in heat input, the CGHAZ grains nearest to the weld become coarser, and the number and size of martensite–austenite (M/A) islands increases, which deteriorates the microstructure and properties of the CGHAZ [5–7]. Therefore, how to improve properties of the heat-affected zone (HAZ) has become a key problem affecting the promotion and application of high heat input welding steel.

Researchers have proposed many ways to improve the properties of the heat-affected zone of high heat input welding steel in order to improve welding efficiency and obtain

excellent HAZ properties. For example, under the premise of low-carbon-equivalent alloy design [8–10], combined oxide metallurgy technology [11], Ti-B technology [12], TiN technology [13], etc., have been suggested. As the control of TiN particles is relatively stable, it has been widely used in industrial production. It is well known that TiN can significantly inhibit the growth of austenite grain boundary migration, thereby improving the microstructure and properties of a simulated CGHAZ; this is called the grain boundary pinning effect [14,15]. The effect of the Ti/N ratio on the microstructure and properties of the CGHAZ is particularly significant. Yan et al. found that a Ti/N ratio greater than stoichiometric accelerated the coarsening rate of TiN particles; a smaller Ti/N ratio promoted the precipitation of TiN particles and inhibited the growth of austenite grains [16]. Zhu et al. believed that different Ti/N ratios have little effect on the average size of precipitates. However, when the Ti/N ratio was closer to the stoichiometric number, the number of TiN precipitates increased. These uniform and fine precipitates could significantly hinder the growth of austenite grains, making the volume fraction of fine austenite grains larger, thus improving the microstructure and properties of the CGHAZ [17,18]. However, most studies of the microstructure and properties of the CGHAZ and Ti/N ratios were only based on welding thermal simulation. Subsequently, simulated samples were analyzed and characterized, and then the effect of the Ti/N ratio on steel for high heat input welding was judged. The study of the dynamic microstructure evolution of the CGHAZ of high heat input welding steel and the Ti/N ratio has not been reported.

In situ observation can realize the real-time observation and analysis of material microstructure. It has gradually become a favorable tool in studies of phase transformation, grain growth and precipitation of steel at high temperature [19–21]. Liu et al. carried out a comparative analysis of the transformation behavior of acicular on the surface and inside of low-carbon manganese steel [22]. Fu et al. modified the prediction model of austenite grain size on the surface of micro-alloy billets based on results of in situ observation [23]. In situ observation is more and more widely used in the field of steel materials, but mostly to observe changes in microstructure, and rarely combined with the characterization of properties for analysis and research.

Therefore, this study systematically examined the influence of the Ti/N ratio on the microstructure and toughness of high heat input welding steel by combining welding thermal simulation with in situ observation. The relationships among welding heat input, microstructure, the microstructure evolution process and toughness are preliminarily established. The research results will help further enrich the design of high heat input welding steel based on TiN theory, and promote the application of high heat input welding steel in engineering.

2. Materials and Methods

In this experiment, steels with different Ti/N ratios were chosen. The chemical compositions of steels are listed in Table 1.

Table 1. Chemical compositions of experimental steels (wt%).

Steels	C	Mn	Si	P	S	Ti	N	Als	Ti/N
A	0.084	1.43	0.26	0.0074	0.0017	0.024	0.0041	0.016	5.85
B	0.084	1.45	0.27	0.0079	0.0017	0.019	0.0045	0.017	4.22
C	0.083	1.45	0.26	0.0067	0.0018	0.013	0.0046	0.015	2.82

The three steels experienced similar thermomechanical processing conditions: a two-stage controlled rolling process. Billets were heated to 1200 °C for 4 h; the rough rolling temperature and second stage temperature were 1100 °C and 920 °C, respectively. After hot rolling, the steels were immediately water cooled to 500–550 °C, and then air cooled to ambient temperature. Finally, the thickness of finished steels was 20 mm.

The simulated samples were cut along the longitudinal direction of the steels and machined to 11 mm × 11 mm × 110 mm. The welding simulation experiments were carried out using a Gleeble-3800. The peak temperature was 1320 °C, which was held for 0.2 s. Next, samples were cooled along different thermal cycles, which equated to 50 kJ/cm, 100 kJ/cm and 150 kJ/cm. Figure 1 shows the corresponding welding thermal cycle curves.

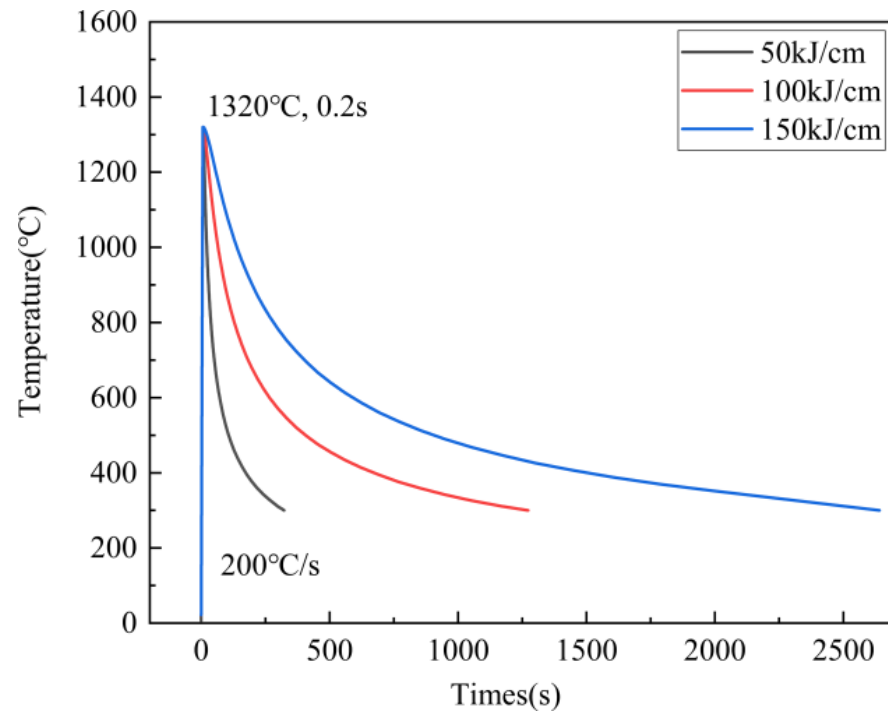


Figure 1. Thermal cycles of simulated CGHAZs.

Metallographic samples were cut from the thermocouples of the welding thermal simulation samples and then ground, polished and etched using 4% nitric acid alcohol. Microstructures were observed using an optical microscope (Axio Observer7). In order to further analyze the changes in crystal structure, electron backscatter diffraction (SUPRA55) was used to study the samples. The specific analysis of electron backscatter diffraction (EBSD) images was performed using HKL Channel 5 software. The samples, after simulation, were machined to 10 mm × 10 mm × 55 mm for impact tests (602-D) at −20 °C. Their impact fracture morphologies were observed using a scanning electron microscope (QUAN 400-HV). Samples were cut at 1/4 thickness of the base metals for transmission electron microscopy observation (Tecnai G2 20). In order to study the quantity and size distribution of TiN particles, 10 transmission electron microscopy (TEM) images, with a total investigated area of 100 μm^2 , were statistically analyzed.

A laser high-temperature confocal microscope (VL2000DX-SVF17SP) was used to observe the microstructures of the samples using approximately the same heat input as the 100 kJ/cm cooling process in the welding thermal simulations. Figure 2 shows the thermal cycle curve of the in situ observation experiment. Samples were heated at 5 °C/s to 1320 °C and held for 0.2 s. Samples were machined into disks (6 mm diameter and 3 mm height) and then polished and put into an alumina crucible. During the whole experiment, the samples were protected by argon to prevent oxidation.

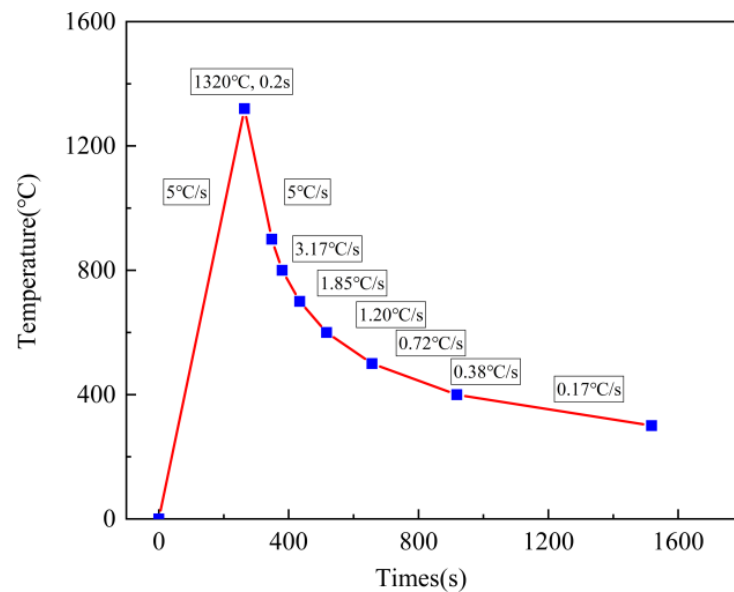


Figure 2. Thermal cycle of in situ observations.

3. Results

3.1. Microstructure

Figure 3 shows the optical microscope (OM) micrographs of CGHAZs of the three steels under different heat inputs. Quantitative metallography was used to obtain statistics regarding the proportion of microstructure constituents, as shown in Figure 4.

When the heat input was 50 kJ/cm, the microstructures of the three steels were mainly composed of bainite (B) and ferrite (F). The amount of bainite in steel A was the highest, accounting for 65.1%, while that in steel C was the least, accounting for only 24.9%. In addition, the ferrite in steels A and B was mainly grain boundary ferrite distributed at the original austenite grain boundary, separating the bainite block. However, the distribution of ferrite in steel C was more homogeneous. When the heat input was 100 kJ/cm, the microstructures of steels A and B were mainly composed of bainite, ferrite and a small amount of pearlite (P). The bainite in steel C disappeared completely. Compared with the microstructure using a heat input of 50 kJ/cm, the content of bainite decreased, while the content of ferrite increased, and a small amount of pearlite appeared. The ferrite in steel C was 33.5% higher than that in steel A. In addition, there were obviously coarse bainite blocks in both steels A and B, and the microstructure of steel C was more homogeneous. When the heat input was 150 kJ/cm, the microstructures of the three steels were composed of ferrite and pearlite, and there was no bainite. Moreover, there was no significant difference in the proportion of the two constituents.

Figure 5 shows the crystallographic characteristics of the simulated CGHAZs of steels with different Ti/N ratios under a heat input of 50 kJ/cm. In the image quality maps, red lines represent low-angle grain boundaries of 2° ~ 5° , and blue lines represent high-angle grain boundaries greater than 15° . The prior austenite grains were divided into many bainite packets, and there were high-angle grain boundaries between packets. The ferrite usually showed high misorientation. In addition, as shown in Figure 5g–i, the number of high-angle grain boundaries gradually increased with a decrease in the Ti/N ratio. Compared with low-angle grain boundaries, high-angle grain boundaries significantly inhibited cleavage crack growth [3,24].

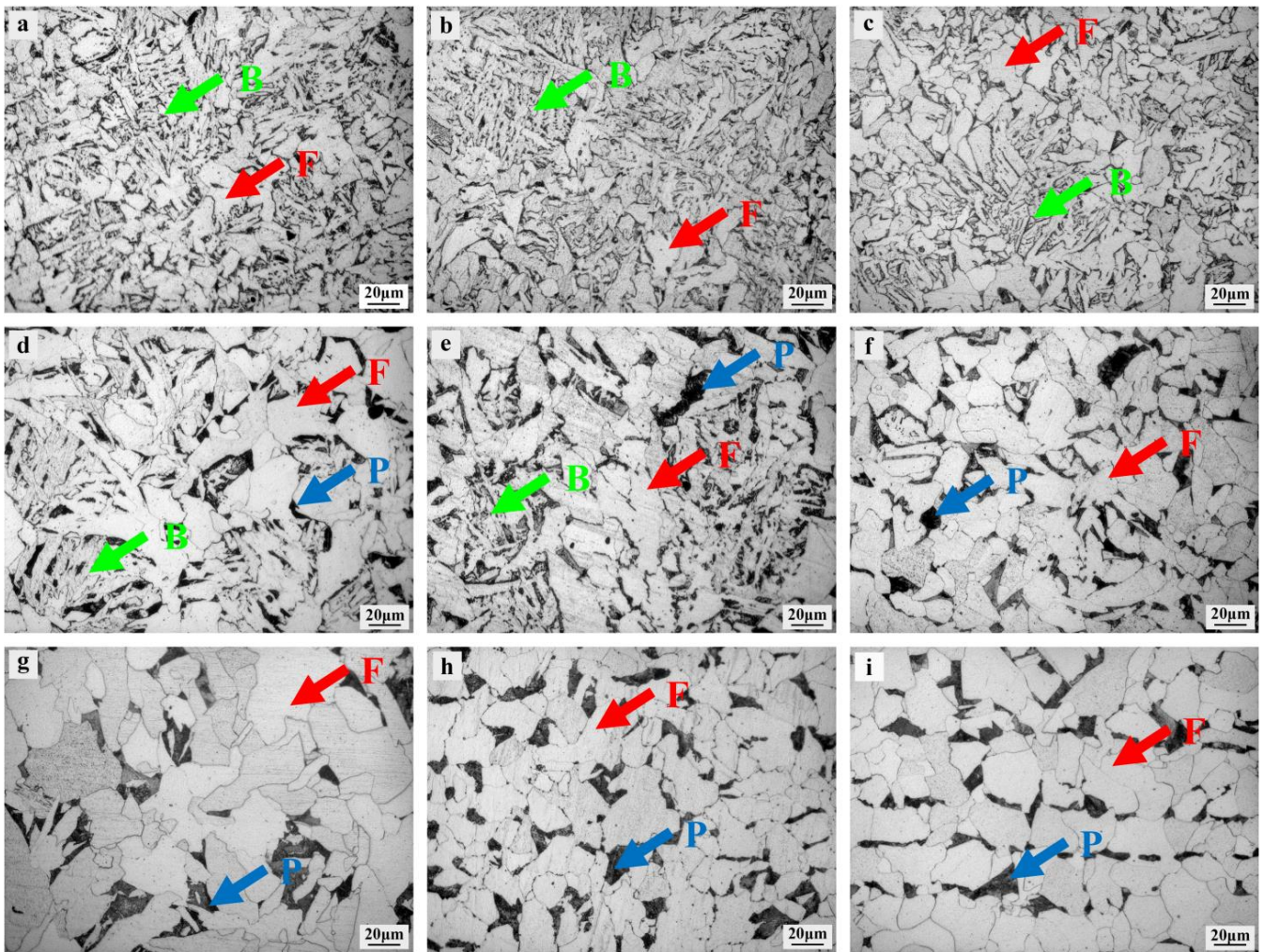


Figure 3. OM micrographs of simulated CGHAZs of high heat input welding steels with different Ti/N ratios under different heat inputs: (a–c): $E = 50 \text{ kJ/cm}$; (d–f): $E = 100 \text{ kJ/cm}$; (g–i): $E = 150 \text{ kJ/cm}$; (a,d,g): $\text{Ti/N} = 5.85$; (b,e,h): $\text{Ti/N} = 4.22$; and (c,f,i): $\text{Ti/N} = 2.82$.

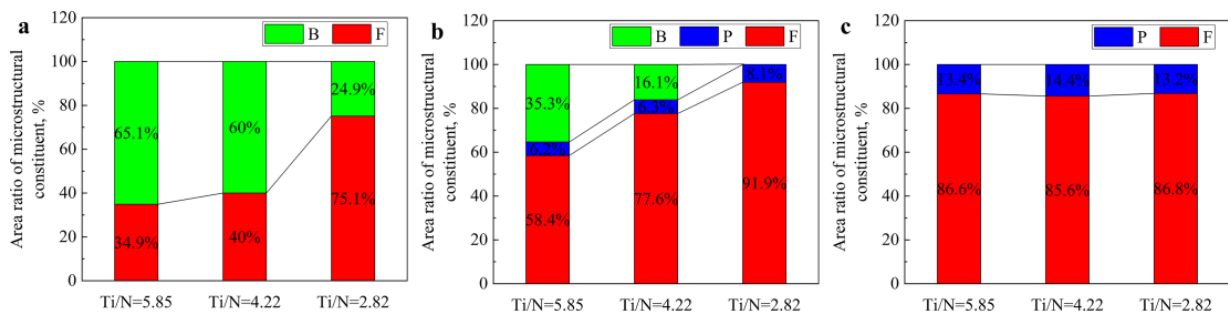


Figure 4. Volume fractions of microstructures of simulated CGHAZs of high heat input welding steels with different Ti/N ratios under different heat inputs: (a) $E = 50 \text{ kJ/cm}$; (b) $E = 100 \text{ kJ/cm}$; and (c) $E = 150 \text{ kJ/cm}$.

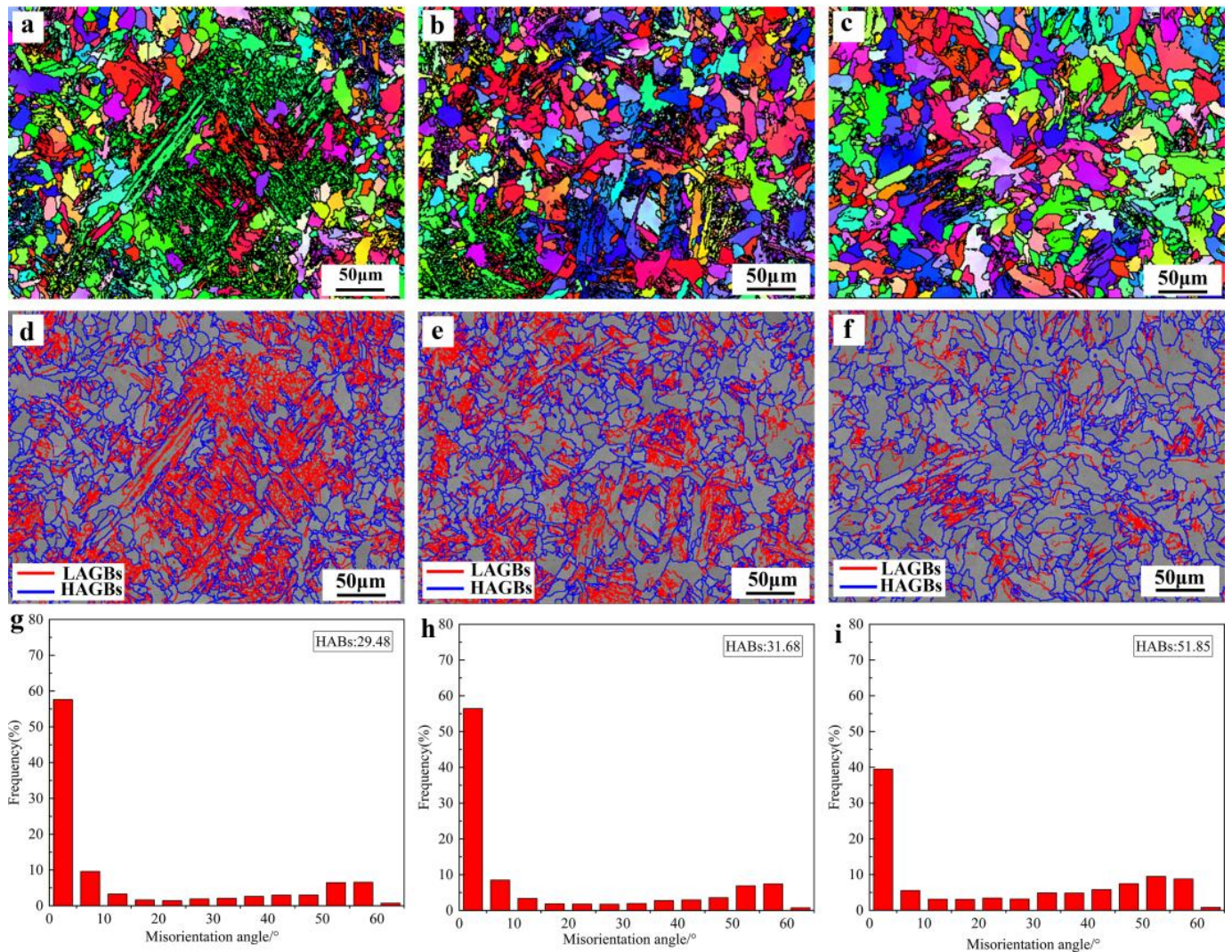


Figure 5. Crystallographic characteristics of simulated CGHAZs of high heat input welding steels with different Ti/N ratios at a heat input of 50 kJ/cm: (a,d,g) Ti/N = 5.85; (b,e,h) Ti/N = 4.22; (c,f,i) Ti/N = 2.82; (a–c) orientation image maps; (d–f) image quality maps with grain boundary misorientation distribution; and (g–i) misorientation angle distribution histograms.

Kernel average misorientation (KAM) color maps of simulated CGHAZs of steels with different Ti/N ratios at a heat input of 50 kJ/cm are shown in Figure 6. KAM values were proportional to geometrically necessary dislocations (GNDs). The greater the GND, the more severe the stress concentration. The characteristic values of KAM maps are shown in Table 2. At a Ti/N ratio of 5.85, the average KAM value was 1.030. However, at a Ti/N ratio of 2.82, the KAM value was only 0.562. Microcracks tended to nucleate at a position of high strain value during the fracture process, resulting in a decrease in properties [25,26].

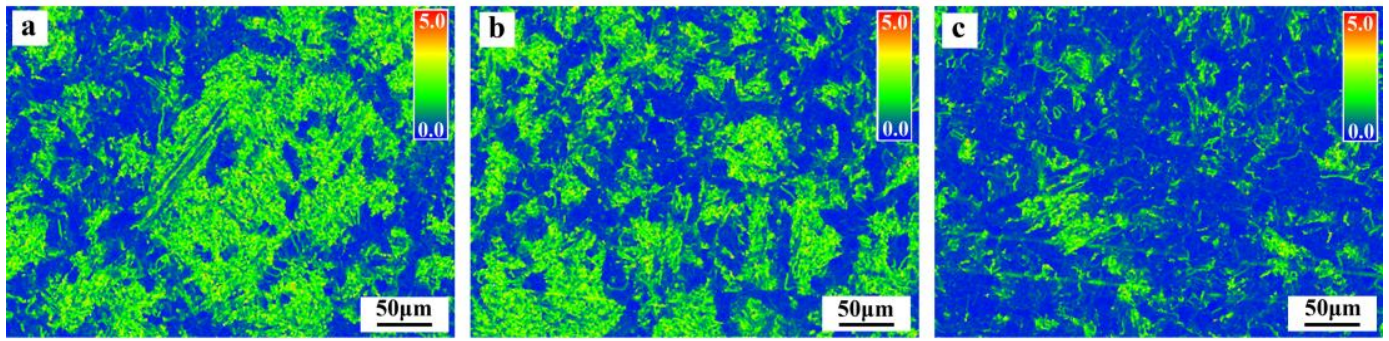


Figure 6. KAM maps of simulated CGHAZs of high heat input welding steels with different Ti/N ratios at a heat input of 50 kJ/cm: (a) Ti/N = 5.85; (b) Ti/N = 4.22; and (c) Ti/N = 2.82.

Table 2. Characteristic values of the KAM maps.

Ti/N	KAM Distribution					Ave
	0°–1°	1°–2°	2°–3°	3°–4°	4°–5°	
5.85	0.570	0.305	0.106	0.017	0.002	1.030
4.22	0.632	0.265	0.086	0.015	0.002	0.939
2.82	0.864	0.108	0.024	0.004	0.001	0.562

3.2. Mechanical Properties

Figure 7 shows the impact toughness of simulated CGHAZs of high heat input welding steels with different Ti/N ratios under different welding heat inputs at −20 °C.

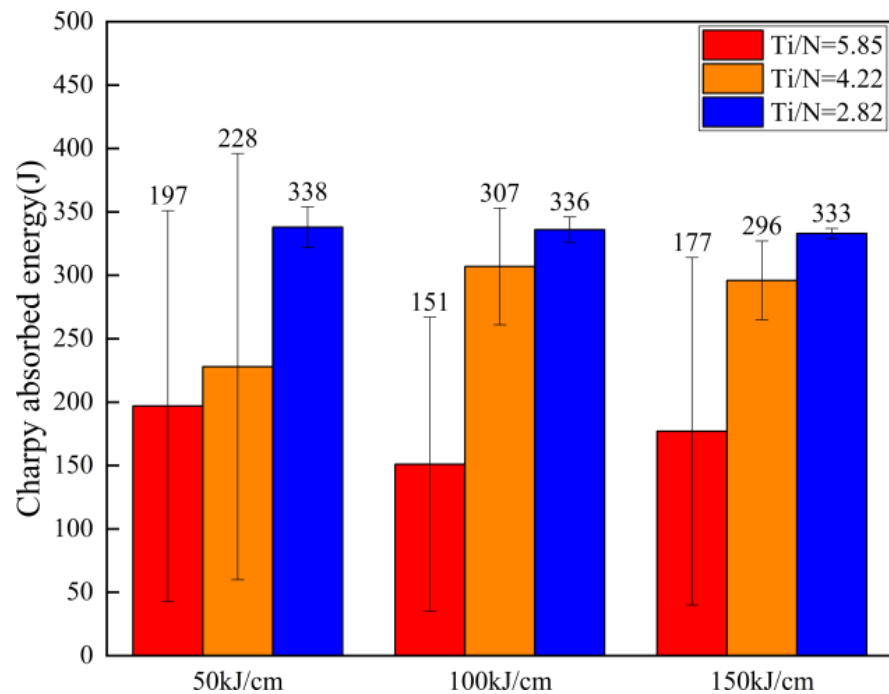


Figure 7. Impact toughness of simulated CGHAZs of high heat welding steels with different Ti/N ratios under different heat inputs.

At this temperature, the average impact toughness of the three steels was high, ranging from 150 to 350 J. The average impact toughness of steel C under different heat inputs was above 330 J, which was obviously higher and more stable. The average impact toughness of steel C still reached 333 J when the heat input was 150 kJ/cm; this was only 5 J lower than

its impact toughness at 50 kJ/cm. The average impact toughness of steel B was slightly lower than that of steel C. The average impact toughness of steel A was the lowest; it was lower than 200 J. The impact energy of steel A showed individual low values at different heat inputs. The impact toughness of steel A significantly fluctuated.

Micrographs of impact fractures in simulated CGHAZs at a heat input of 50 kJ/cm are displayed in Figure 8. The brittle sample of steel A simulated CGHAZ was selected for observation; there was almost no ductile fracture area in the fracture surface, including a large number of cleavage facets. Nevertheless, fracture surfaces were composed of large and deep dimples for simulated CGHAZs impact fractures of steels B and C, which were obvious ductile fracture modes.

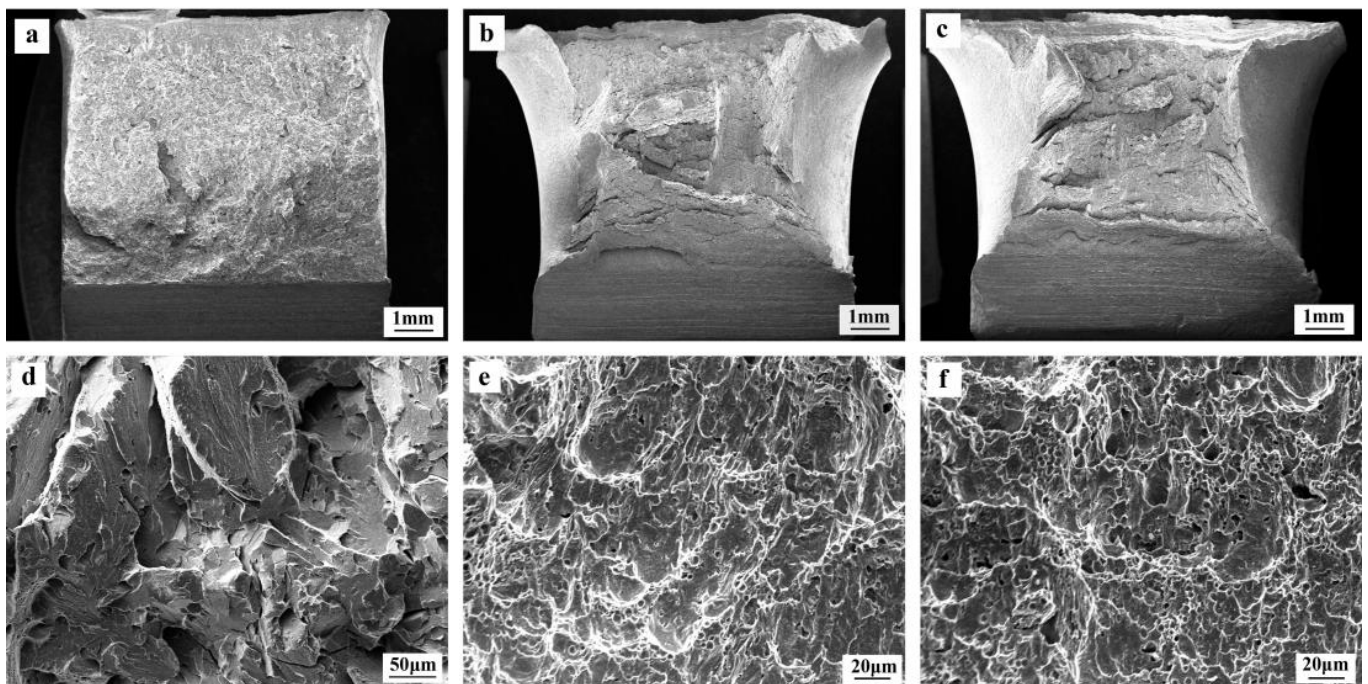


Figure 8. Impact fracture micrographs of simulated CGHAZs of high heat input welding steels with different Ti/N ratios at a heat input of 50 kJ/cm: (a,d) Ti/N = 5.85; (b,e) Ti/N = 4.22; and (c,f) Ti/N = 2.82.

3.3. In Situ Observation

Figure 9 shows in situ observations of microstructure transformations of high heat input welding steels with different Ti/N ratios in the cooling stage during the welding thermal cycle. When the cooling temperature was 899 °C, the microstructures of the three steels were austenite. The grains in steels A and B grew obviously abnormal. However, the austenite grains in steel C were significantly more uniform. With a decrease in temperature, lath ferrite gradually appeared in the three steels. The temperature at which lath ferrite appeared also gradually decreased. Lath ferrites were found at 701 °C, 696 °C and 672 °C in steels A, B and C, respectively. The temperature of ferrite in steel A was 29 °C higher than it was in steel C. The higher the formation temperature of lath ferrite, the more sufficient time and space were available for lath ferrite to grow, resulting in uneven microstructures.

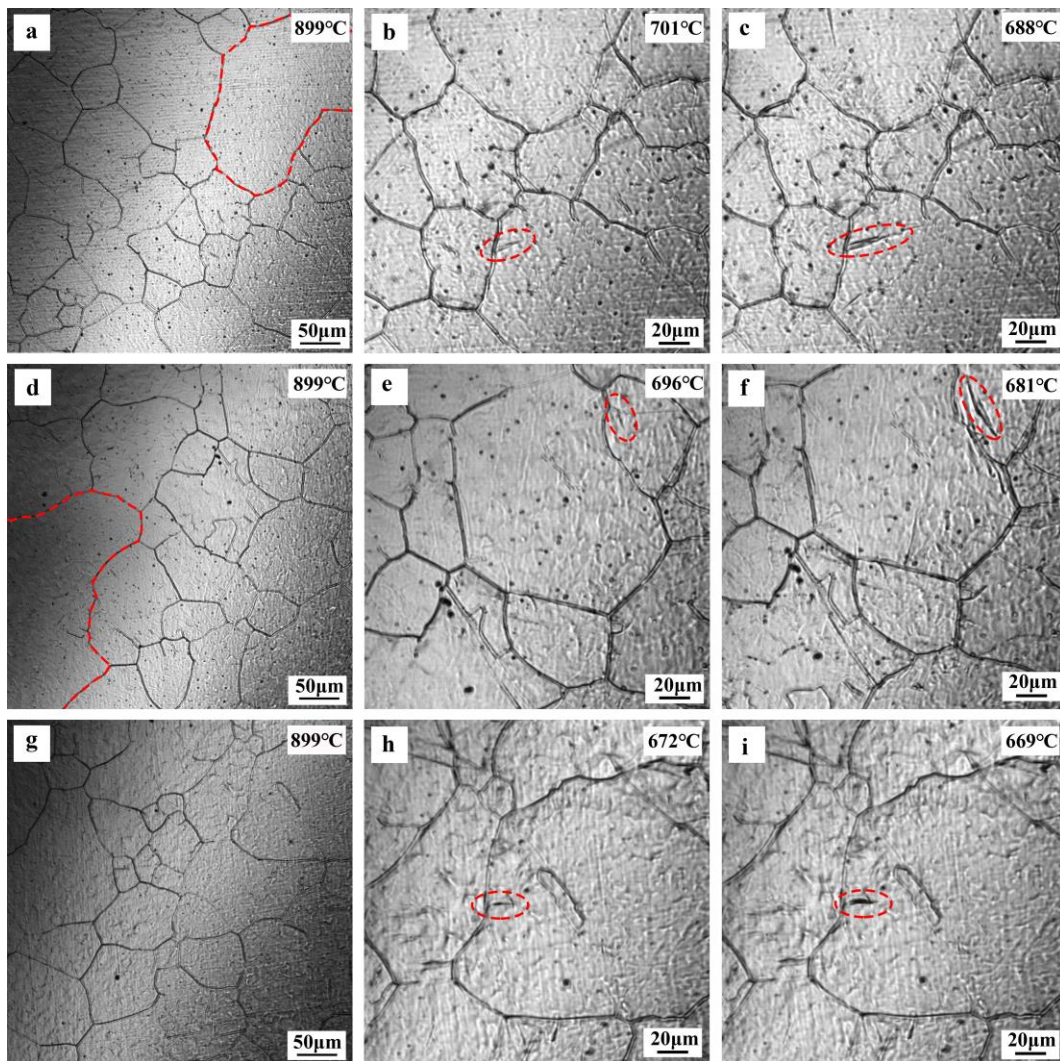


Figure 9. In situ observations of simulated CGHAZs microstructures of high heat input welding steels with different Ti/N ratios during the cooling process: (a–c) Ti/N = 5.85; (d–f) Ti/N = 4.22; and (g–i) Ti/N = 2.82.

4. Discussion

4.1. Effect of the Ti/N Ratio on Austenite Grain Growth

It is generally accepted that TiN particles inhibit austenite grain boundary migration. When the products of Ti content and N content are greater than the solubility product at this temperature, TiN particles precipitate. The solubility product for TiN in austenite is given by Equation (1) [27,28]:

$$\text{Lg}\{[\text{Ti}_{\text{dissolved}}][\text{N}_{\text{dissolved}}]\}_{\gamma} = 4.35 - 14890/T, \quad (1)$$

where $[\text{Ti}_{\text{dissolved}}]$ and $[\text{N}_{\text{dissolved}}]$ are concentrations of Ti and N dissolved in austenite, respectively, and T is the absolute temperature.

The solidus and liquidus temperatures of the three steels were calculated using Thermo-Calc software in the range of 1482–1520 °C. Combined with Equation (1), the relationships between dissolved Ti and dissolved N contents at different peak temperatures were calculated, as shown in Figure 10. It was assumed that all Ti and N in steels with different Ti/N ratios could be dissolved in austenite. For the steel with a Ti/N ratio of 2.82, TiN particles did not start to precipitate until solidification. However, for steels with Ti/N ratios of 4.22 and 5.85, TiN particles started to precipitate before complete solidification.

The diffusion rate of elements in liquid was faster; TiN particles grew freely and coarsened faster. In addition, due to the same [N] content in the three steels, the higher the Ti/N ratio was, the greater the [Ti] content was, which promoted the nucleation and growth of TiN particles. However, the diffusion rate of elements in solid was slower, which was not conducive to the growth of TiN particles; therefore, more uniformly dispersed TiN particles formed.

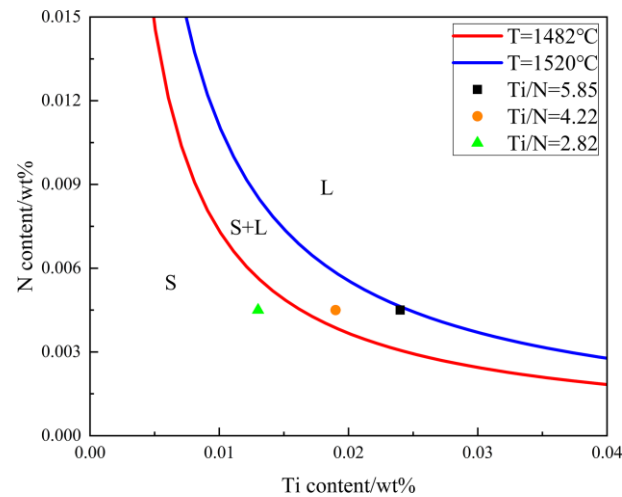


Figure 10. Relationships between the contents of Ti and N at different peak temperatures.

Figure 11 shows TEM microstructures and size distributions of precipitates in high heat input welding steels with different Ti/N ratios.

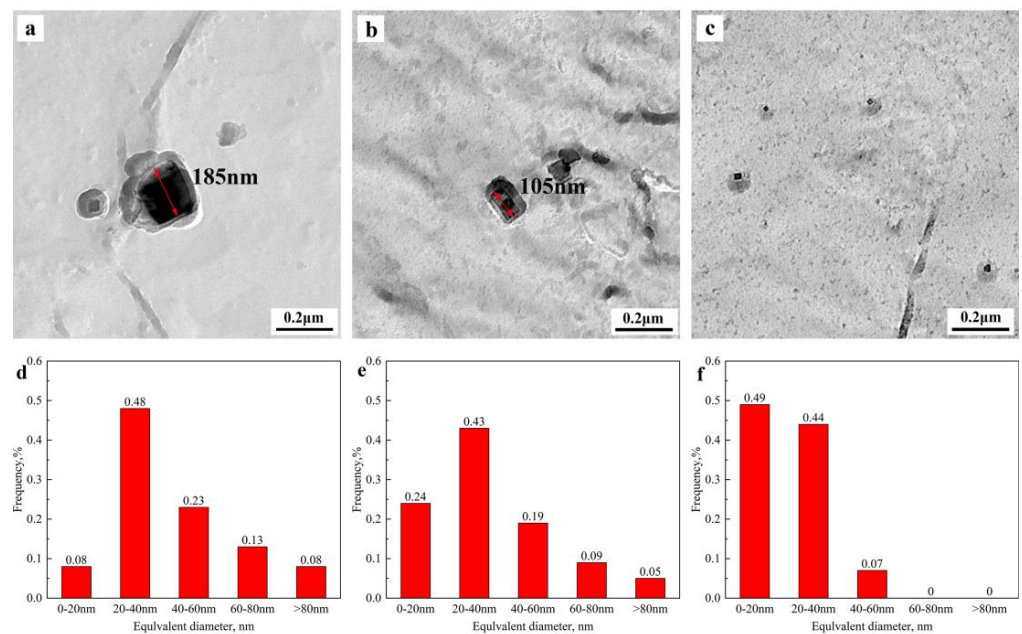


Figure 11. Size distributions of precipitates in high heat input welding steels with different Ti/N ratios: (a,d) Ti/N = 5.85; (b,e) Ti/N = 4.22; and (c,f) Ti/N = 2.82.

Compared with steels A and B, TiN particles in steel C were smaller and more dispersed. TiN particles larger than 100 nm were found in steel A and steel B; the diameter of TiN particles in steel C was mainly less than 40 nm. These TiN particles significantly inhibited austenite grain boundary migration to refine grains. As shown in Figure 9, coarse TiN particles weakened pinning of the grain boundary, resulting in the abnormal growth of austenite grains.

4.2. Effect of the Ti/N Ratio on CGHAZ Microstructure and Toughness

The microstructure and properties of the simulated CGHAZ for high heat input welding steels indicate that TiN particles had a strong grain refinement strengthening effect, which was mainly due to the inhibiting behavior of TiN particles on austenite grain boundary migration. Under the condition of high heat input welding, when the Ti/N ratio was low, fine dispersed TiN particles hindered the movement of the austenitic grain boundary, which significantly affected austenitic grain growth. The finer the prior austenite grains, the more grain boundaries there were in unit volume. The free energy of phase transformation at the grain boundary was high, so ferrite was preferentially formed at the grain boundary, which meant that the proportion of ductile structure in the CGHAZ correspondingly increased [29]. In addition, the grain boundary misorientation angle was also a key factor, leading to significant differences in impact toughness. The more numerous the prior austenite grains were, the higher the content of high-angle grain boundaries. During impact processing, high-angle grain boundaries played a strong role in hindering crack propagation and absorbing more expansion energy, thus leading to an improvement in the impact toughness of the simulated CGHAZ [30].

When the Ti/N ratio was too high, large TiN particles formed in the steel. Coarse TiN particles weaken the ability of pinning austenite grain boundary movement; as a result, the final microstructure coarsened. In addition, during the phase transformation of the steel with a high Ti/N ratio, coarse TiN particles acted as nucleation particles to promote the nucleation and growth of lath ferrite [31]. As a result, the nucleation temperature of lath ferrite increased, and the lath ferrite formed at high temperature had sufficient time and space to grow, resulting in a decrease in the CGHAZ structure's uniformity, which significantly deteriorated the toughness of the CGHAZ. In addition, a higher alloy content and welding heat input promoted the formation and coarsening of martensite–austenite (M-A) components, which were the initial sources of cracks, further leading to a decrease in impact energy [32,33].

The combination of welding thermal simulation and in situ observation more systematically and comprehensively showed the effect of the Ti/N ratio on simulated CGHAZ microstructure evolution and low-temperature impact toughness, which enriched the design theory of high heat input welding steel and provided solid data support for steel designed based on TiN theory.

5. Conclusions

In this study, the effect of different Ti/N ratios on the microstructure evolution and low-temperature impact toughness of high heat input welding steel under different heat inputs was investigated using a combination of welding thermal simulations and in situ observations. The main conclusions were as follows:

- (1) A lower Ti/N ratio reduced the size of TiN particles, which made the distribution of TiN particles more uniform. A higher Ti/N ratio promoted the appearance of coarse TiN particles in the steel.
- (2) A lower Ti/N ratio refined the microstructure of the CGHAZ, increased the proportion of ductile microstructure and the content of high-angle grain boundaries, and reduced the generation of local high strain structure.
- (3) The coarse TiN particles formed by a higher Ti/N ratio weakened the pinning of the grain boundary, resulting in an increase in the formation temperature of lath ferrite and the coarsening of the CGHAZ microstructure.
- (4) For the steel with a Ti/N ratio of 2.82, the average impact toughness was higher and more stable. For the steel with a Ti/N of 5.85, the impact toughness was lower and clearly fluctuated.

Author Contributions: Conceptualization, J.L.; investigation, J.L., J.W., F.H., K.F., Z.Z. and Y.W.; methodology, J.W. and K.F.; data curation, J.L. and F.H.; and writing—original draft, J.L. All authors have read and agreed to the published version of the manuscript.

Funding: This research received no external funding.

Institutional Review Board Statement: Not applicable.

Informed Consent Statement: Not applicable.

Data Availability Statement: Data are available on request from the corresponding author.

Conflicts of Interest: The authors declare no conflict of interest.

References

1. Shen, Y.; Leng, J.; Wang, C. On the heterogeneous microstructure development in the welded joint of 12MnNiVR pressure vessel steel subjected to high heat input electrogas welding. *J. Mater. Sci. Technol.* **2019**, *35*, 1747–1752. [[CrossRef](#)]
2. Porcaro, R.R.; Faria, G.L.; Godefroid, L.B.; Apolonio, G.R.; Cândido, L.C.; Pinto, E.S. Microstructure and mechanical properties of a flash butt welded pearlitic rail. *J. Mater. Process. Technol.* **2019**, *270*, 20–27. [[CrossRef](#)]
3. Shi, Z.; Wang, R.; Su, H.; Chai, F.; Wang, Q.; Yang, C. Effect of nitrogen content on the second phase particles in V–Ti microalloyed shipbuilding steel during weld thermal cycling. *Mater. Des.* **2016**, *96*, 241–250. [[CrossRef](#)]
4. Liu, Z.; Song, B.; Mao, J. Effect of Ca on the evolution of inclusions and the formation of acicular ferrite in Ti–Mg killed EH36 steel. *Ironmak. Steelmak.* **2021**, *48*, 1115–1122. [[CrossRef](#)]
5. Lee, C.H.; Bhadeshia, H.K.D.H.; Lee, H.C. Effect of plastic deformation on the formation of acicular ferrite. *Mater. Sci. Eng. A* **2003**, *360*, 249–257. [[CrossRef](#)]
6. Kojima, A.; Kiyose, A.; Uemori, R.; Minagawa, M.; Hoshino, M.; Nakashima, T.; Ishida, K.; Yasui, H. Super High HAZ Toughness Technology with Fine Microstructure Imparted by Fine Particles. *Nippon Steel Tech. Rep.* **2004**, *90*, 2–6.
7. Zou, X.; Sun, J.; Matsuura, H.; Wang, C. Profiling Microstructure Evolution Roadmap in Heat-Affected Zones of EH36 Shipbuilding Steel Under Controlled Thermal Simulation. *Met. Mater. Trans. A* **2020**, *51*, 3392–3397. [[CrossRef](#)]
8. Fan, H.; Shi, G.; Peng, T.; Wang, Q.; Wang, L.; Wang, Q.; Zhang, F. N-induced microstructure refinement and toughness improvement in the coarse grain heat-affected zone of a low carbon Mo–V–Ti–B steel subjected to a high heat input welding thermal cycle. *Mater. Sci. Eng. A* **2021**, *824*, 141799. [[CrossRef](#)]
9. Qiao, M.; Fan, H.; Shi, G.; Wang, L.; Wang, Q.; Wang, Q.; Liu, R. Effect of Welding Heat Input on Microstructure and Impact Toughness in the Simulated CGHAZ of Low Carbon Mo–V–Ti–N–B Steel. *Metals* **2021**, *11*, 1997. [[CrossRef](#)]
10. Zhang, J.; Xin, W.; Ge, Z.; Luo, G.; Peng, J. Effect of high heat input welding on the microstructures, precipitates and mechanical properties in the simulated coarse grained heat affected zone of a low carbon Nb–V–Ti–N microalloyed steel. *Mater. Charact.* **2023**, *199*, 112849. [[CrossRef](#)]
11. Wang, X.; Wang, C.; Kang, J.; Wang, G.; Misra, D.; Yuan, G. Relationship Between Impact Toughness and Microstructure for the As-Rolled and Simulated HAZ of Low-Carbon Steel Containing Ti–Ca Oxide Particles. *Met. Mater. Trans. A* **2020**, *51*, 2927–2938. [[CrossRef](#)]
12. Kimura, T.; Sumi, H.; Kitani, Y. High tensile strength steel plates and welding consumables for architectural construction with excellent toughness in welded joint–“JFE EWEL” technology for excellent quality in HAZ of high heat input welded joints. *JFE Tech. Rep.* **2005**, *5*, 45–52.
13. Shi, M.H.; Du, K.; Gao, P.; Zhang, J. Microstructure Evolution and Toughness Variation of Simulation HAZ with Large Heat Input Welding for E40 Ship Plate Steel. *IOP Conf. Ser. Mater. Sci. Eng.* **2018**, *382*, 032010. [[CrossRef](#)]
14. Tomita, Y.; Saito, N.; Tsuzuki, T.; Tokunaga, Y.; Okamoto, K. Improvement in HAZ Toughness of Steel by TiN–MnS Addition. *ISIJ Int.* **1994**, *34*, 829–835. [[CrossRef](#)]
15. Wan, X.-l.; Wu, K.-M.; Huang, G.; Wei, R.; Cheng, L. In situ observation of austenite grain growth behavior in the simulated coarse-grained heat-affected zone of Ti-microalloyed steels. *Int. J. Miner. Met. Mater.* **2014**, *21*, 878–885. [[CrossRef](#)]
16. Yan, W.; Shan, Y.Y.; Yang, K. Effect of TiN inclusions on the impact toughness of low-carbon microalloyed steels. *Met. Mater. Trans. A* **2006**, *37*, 2147–2158. [[CrossRef](#)]
17. Zhu, Z.X.; Marimuthu, M.; Kuzmikova, L.; Li, H.J.; Barbaro, F.; Zheng, L.; Bai, M.Z.; Jones, C. Influence of Ti/N ratio on simulated CGHAZ microstructure and toughness in X70 steels. *Sci. Technol. Weld. Join.* **2013**, *18*, 45–51. [[CrossRef](#)]
18. Li, X.; Fan, Y.; Ma, X.; Subramanian, S.V.; Shang, C. Influence of Martensite–Austenite constituents formed at different intercritical temperatures on toughness. *Mater. Des.* **2015**, *67*, 457–463. [[CrossRef](#)]
19. Zhang, D.; Terasaki, H.; Komizo, Y.I. In situ observation of the formation of intragranular acicular ferrite at non-metallic inclusions in C–Mn steel. *Acta Mater.* **2010**, *58*, 1369–1378. [[CrossRef](#)]
20. Wan, X.; Wu, K.; Cheng, L.; Wei, R. In-situ Observations of Acicular Ferrite Growth Behavior in the Simulated Coarse-grained Heat-affected Zone of High-strength Low-alloy Steels. *ISIJ Int.* **2015**, *55*, 679–685. [[CrossRef](#)]
21. Zou, X.; Sun, J.; Matsuura, H.; Wang, C. In Situ Observation of the Nucleation and Growth of Ferrite Laths in the Heat-Affected Zone of EH36–Mg Shipbuilding Steel Subjected to Different Heat Inputs. *Met. Mater. Trans. B* **2018**, *49*, 2168–2173. [[CrossRef](#)]
22. Liu, X.; Yuan, G.; Misra, R.D.; Wang, G. A Comparative Study of Acicular Ferrite Transformation Behavior between Surface and Interior in a Low C–Mn Steel by HT-LSCM. *Metals* **2021**, *11*, 699. [[CrossRef](#)]
23. Fu, D.C.; Wen, G.H.; Zhu, X.Q.; Guo, J.L.; Tang, P. Modification for prediction model of austenite grain size at surface of microalloyed steel slabs based on in situ observation. *J. Iron Steel Res. Int.* **2021**, *28*, 1133–1140. [[CrossRef](#)]

24. Zhang, Y.; Xiao, J.; Liu, W.; Zhao, A. Effect of Welding Peak Temperature on Microstructure and Impact Toughness of Heat-Affected Zone of Q690 High Strength Bridge Steel. *Materials* **2021**, *14*, 2981. [[CrossRef](#)] [[PubMed](#)]
25. Tong, M.; Di, X.; Li, C.; Wang, D. Toughening mechanism of inter-critical heat-affected zone in a 690 MPa grade rack plate steel. *Mater. Charact.* **2018**, *144*, 631–640. [[CrossRef](#)]
26. Zheng, C.; Liu, Q.; Zheng, S.; Chong, X.; Jiang, Y.; Feng, J. Effect of solution treatment on mechanical properties and microstructure of welded joints of Fe-29Mn-9Al-0.9C low-density steel. *J. Micromech. Mol. Phys.* **2020**, *5*, 2050006. [[CrossRef](#)]
27. Inoue, K.; Ohnuma, I.; Ohtani, H.; Ishida, K.; Nishizawa, T. Solubility Product of TiN in Austenite. *ISIJ Int.* **1998**, *38*, 991–997. [[CrossRef](#)]
28. Chen, H.; Gamsjäger, E.; Schider, S.; Khanbareh, H.; van der Zwaag, S. In situ observation of austenite–ferrite interface migration in a lean Mn steel during cyclic partial phase transformations. *Acta Mater.* **2013**, *61*, 2414–2424. [[CrossRef](#)]
29. Yamamoto, S.; Yokoyama, H.; Yamada, K.; Niikura, M. Effects of the Austenite Grain Size and Deformation in the Unrecrystallized Austenite Region on Bainite Transformation Behavior and Microstructure. *ISIJ Int.* **1995**, *35*, 1020–1026. [[CrossRef](#)]
30. Li, X.; Lu, G.; Wang, Q.; Zhao, J.; Xie, Z.; Misra, R.D.; Shang, C. The Effects of Prior Austenite Grain Refinement on Strength and Toughness of High-Strength Low-Alloy Steel. *Metals* **2021**, *12*, 28. [[CrossRef](#)]
31. Mu, W.; Jönsson, P.G.; Nakajima, K. Prediction of intragranular ferrite nucleation from TiO, TiN, and VN inclusions. *J. Mater. Sci.* **2015**, *51*, 2168–2180. [[CrossRef](#)]
32. Jorge, J.C.F.; Bott, I.S.; Souza, L.F.G.; Mendes, M.C.; Araújo, L.S.; Evans, G.M. Mechanical and microstructural behavior of C-Mn steel weld deposits with varying titanium contents. *J. Mater. Res. Technol.* **2019**, *8*, 4659–4671. [[CrossRef](#)]
33. Yu, H.; Wu, K.; Dong, B.; Liu, J.; Liu, Z.; Xiao, D.; Jin, X.; Liu, H.; Tai, M. Effect of Heat-Input on Microstructure and Toughness of CGHAZ in a High-Nb-Content Microalloyed HSLA Steel. *Materials* **2022**, *15*, 3588. [[CrossRef](#)]

Disclaimer/Publisher’s Note: The statements, opinions and data contained in all publications are solely those of the individual author(s) and contributor(s) and not of MDPI and/or the editor(s). MDPI and/or the editor(s) disclaim responsibility for any injury to people or property resulting from any ideas, methods, instructions or products referred to in the content.